# Clusters of cerebellar Purkinje cells control their afferent climbing fiber discharge

Joseph Chaumont[a], Nicolas Guyon[b], Antoine M. Valera[a], Guillaume P. Dugué[b], Daniela Popa[b], Paikan Marcaggi[b], Vanessa Gautheron[c], Sophie Reibel-Foisset[d], Stéphane Dieudonné[b], Aline Stephan[e], Michel Barrot[a], Jean-Christophe Cassel[f], Jean-Luc Dupont[a], Frédéric Doussau[a], Bernard Poulain[a], Fekrije Selimi[c,1], Clément Léna[b,1], and Philippe Isope[a,1,2]

[a]Institut des Neurosciences Cellulaires et Intégratives, Centre National de la Recherche Scientifique, Unité Propre de Recherche 3212, Université de Strasbourg, 67084 Strasbourg, France; [b]Institut de Biologie de l'Ecole Normale Supérieure, Centre National de la Recherche Scientifique, Unité Mixte de Recherche 8197, Institut National de la Santé et de la Recherche Médicale, Unité 1024, 75005 Paris, France; [c]Center for Interdisciplinary Research in Biology, Collège de France, Centre National de la Recherche Scientifique, Unité Mixte de Recherche 7241, Institut National de la Santé et de la Recherche Médicale, Unité 1050, 75005 Paris, France; [d]Chronobiotron, Unité Mixte de Service 3415, Centre National pour la Recherche Scientifique, Université de Strasbourg, 67084 Strasbourg, France; [e]Institut de Génétique Moléculaire et Cellulaire, Centre National de la Recherche Scientifique, Unité Mixte de Recherche 7104, Institut National de la Santé et de la Recherche Médicale, Unité 964, Université de Strasbourg, 67400 Illkirch, France; and [f]Laboratoire de Neurosciences Cognitives et Adaptatives, Centre National de la Recherche Scientifique, Unité Mixte de Recherche 7364, Université de Strasbourg, 67084 Strasbourg, France

Edited by Shigetada Nakanishi, Osaka Bioscience Institute, Suita, Japan, and approved August 29, 2013 (received for review February 5, 2013)

**Climbing fibers, the projections from the inferior olive to the cerebellar cortex, carry sensorimotor error and clock signals that trigger motor learning by controlling cerebellar Purkinje cell synaptic plasticity and discharge. Purkinje cells target the deep cerebellar nuclei, which are the output of the cerebellum and include an inhibitory GABAergic projection to the inferior olive. This pathway identifies a potential closed loop in the olivo-cortico-nuclear network. Therefore, sets of Purkinje cells may phasically control their own climbing fiber afferents. Here, using in vitro and in vivo recordings, we describe a genetically modified mouse model that allows the specific optogenetic control of Purkinje cell discharge. Tetrode recordings in the cerebellar nuclei demonstrate that focal stimulations of Purkinje cells strongly inhibit spatially restricted sets of cerebellar nuclear neurons. Strikingly, such stimulations trigger delayed climbing-fiber input signals in the stimulated Purkinje cells. Therefore, our results demonstrate that Purkinje cells phasically control the discharge of their own olivary afferents and thus might participate in the regulation of cerebellar motor learning.**

motor control | olivo-cerebellar loop | complex spikes

The cerebellar cortex is involved in a wealth of functions, from the control of posture to higher cognitive processes (1–3). Purkinje cells (PCs) are key processing units of the cerebellar cortex (4): each PC receives more than 175,000 parallel fiber synaptic inputs carrying information about the ongoing sensory-motor context. It also receives a single inferior olive afferent, the climbing fiber, which triggers a complex spike (CS), modulates PC firing (5), controls synaptic input plasticity, and has been proposed to carry error and clock signals to the cerebellum (2, 4–8). PCs are grouped in multiple parasagittal microzones, each receiving projections from separate areas of the inferior olive and projecting to subregions of the cerebellar nuclei (CN) (9–12). In the CN, PCs make inhibitory contacts on excitatory neurons that project to various premotor areas and propagate cerebellar computations to the motor system. Anatomical evidence indicates that PC terminals also contact CN inhibitory neurons that target inferior olive cells (13, 14). This nucleo-olivary pathway is topographically organized in multiple parallel projections to the inferior olive subnuclei (15), suggesting the existence of closed olivary-cortico-nuclear loops. Therefore, the discharge of a population of PCs in a microzone might not only shape the output of the cerebellum but also control its afferent climbing-fiber signal. Previous studies have shown that stimulation of the nucleo-olivary pathway significantly reduces olivary cell firing (16–18) and that pharmacological and genetic manipulations of PCs or olivary cell activity induce reciprocal modulations of the firing rate of PCs and climbing fibers (19, 20). These results indicate that PCs may tonically modulate the nucleo-olivary pathway. However, whether the cerebellar cortex can phasically recruit this pathway and whether this circuit functions as a closed loop is currently unknown. We thus set out to study the impact of phasic stimulations of PCs on cortico-nucleo-olivary loops. To control selectively PC firing rates, we engineered a mouse line expressing Channelrhodopsin-2 (ChR2) specifically in PCs. By combining optogenetic stimulation and in vivo electrophysiological recordings, we show that stimulating a set of PCs in a region of the cerebellar cortex triggers a restricted inhibition in the cerebellar nuclei and a transient disinhibition of the inferior olive cells that project to this set of PCs.

## Results

**L7-ChR2-eYFP Mice Engineering.** A genetically modified mouse (L7-ChR2) that expresses ChR2(H134R)-Yellow Fluorescent Protein (YFP) under the control of the regulatory elements of the *pcp2* gene was created using the bacterial artificial chromosome modification strategy (*SI Methods*, Fig. 1*A*, and Fig. S1*A*) (21). Specific expression of the ChR2-YFP fusion protein in all PCs of the cerebellar cortex was detected by YFP fluorescence on cerebellar sections and confirmed by anti-calbindin immunostaining (Fig. 1*B* and Fig. S1*B*). GABA immunostaining and whole-cell patch-clamp recordings in acute cerebellar slices showed no expression in molecular layer interneurons or Golgi cells (Fig. 1*D*). Behavioral tests were performed to assess motor performance of the mutant mice. No difference was found

### Significance

The inferior olive, one of the major source of inputs to the cerebellum, sends climbing fibers to Purkinje cells, the key processing units of cerebellar-dependent motor control. Using an optogenetic strategy, we demonstrate that Purkinje cells disinhibit their climbing-fiber afferents via a poly-synaptic circuit. These findings identify a functional closed-loop organization in the olivo-cerebellar circuits that is potentially important for cerebellar motor learning.

Author contributions: F.S., C.L., and P.I. designed research; J.C., N.G., A.M.V., G.P.D., P.M., V.G., S.R.-F., F.D., F.S., and P.I. performed research; S.D., A.S., M.B., J.-C.C., B.P., F.S., and C.L. contributed new reagents/analytic tools; J.C., G.P.D., D.P., J.-L.D., F.S., C.L., and P.I. analyzed data; and J.C., C.L., and P.I. wrote the paper.

The authors declare no conflict of interest.

This article is a PNAS Direct Submission.

[1]F.S., C.L., and P.I. contributed equally to this work.

[2]To whom correspondence should be addressed. E-mail: philippe.isope@inci-cnrs.unistra.fr.

This article contains supporting information online at www.pnas.org/lookup/suppl/doi:10.1073/pnas.1302310110/-/DCSupplemental.

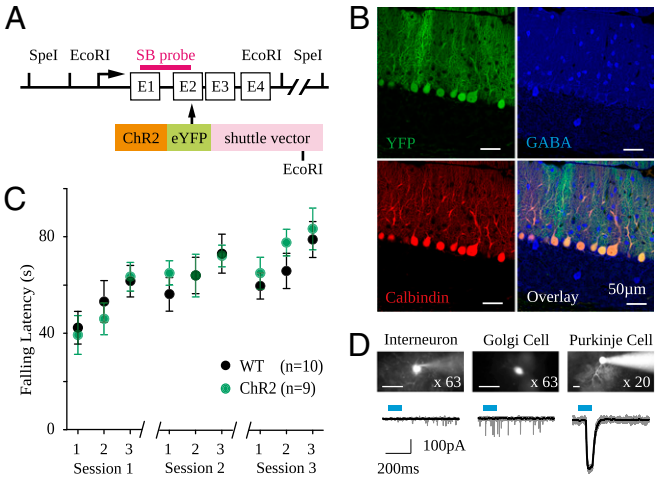


**Fig. 1.** Generation and characterization of L7-ChR2(H134R)-eYFP mice. (*A*) Diagram of the modified BAC containing the ChR2(H134R)-eYFP cDNA under the control of the L7/pcp2 gene regulatory elements. (*B*) Transgene expression monitored by YFP fluorescence in cerebellar sections (*Upper Left*); (*Lower Left*) calbindin immunolabeling; (*Upper Right*) GABA immunolabeling; (*Lower Right*) overlay. (*C*) Falling latencies in the rotarod test during three sessions of three trials at 0–45 rpm (tested by multifactorial ANOVA, $P = 0.392$; WT, $n = 10$; ChR2, $n = 9$). (*D*) Molecular layer interneurons, Golgi cells, and Purkinje cells recorded in acute cerebellar slices visualized using Alexa 594 in the pipette and wide-field illumination at 473 nm. (Scale bar: 20 µm.) No current was observed in molecular layer interneurons ($n = 4$) and Golgi cells ($n = 6$).

between L7-ChR2 mice and wild-type littermates (Fig. 1*C*), indicating that this transgene expression does not perturb motor functions.

**Control of Purkinje Cells by Light.** To characterize PC activation by ChR2, in vitro recordings were performed on acute cerebellar slices using whole-cell patch-clamp. Wide-field illumination with blue light (Fig. 2*A* and *SI Methods*) systematically activated an inward current in all PCs tested ($n = 65$; Fig. 2 *B–D*). By restricting the field of illumination (*SI Methods*), we could show that ChR2 channels are expressed throughout PC dendrites (Fig. 2*B*) and estimate their density to be 150–300 channels per µm$^2$ illuminated [Fig. S2, assuming a unitary conductance of 100 fS (22)]. We then set out to characterize the current induced in PCs by illumination as a function of irradiance and pulse duration. For a pulse duration of 1 ms, increasing irradiance enhanced the amplitude of the photocurrent up to several hundred picoamps (Fig. 2*C* and *SI Methods*) with a decay time constant of 17.3 ± 8.5 ms ($n = 11$). For longer pulses (100 ms), the current rapidly desensitized to a stationary current at 58 ± 3% of the peak for stimulation frequency below 0.05 Hz ($n = 5$) (Fig. 2 *C*, *iv*), in agreement with previous work (23). The pulse frequency used in most of the experiments reported in this work was above 0.05 Hz, leading to a smaller peak current but a similar stationary current (Fig. 2*C*). Current-clamp recordings showed that light-evoked current carrying a charge above 14.7 ± 10 pC ($n = 4$) elicited an action potential in PCs (Vm = −60 mV) and that action potentials were repeated during burst illuminations of up to 10 Hz for irradiance above 8 mW/mm$^2$ (Fig. 2*D*). These results demonstrate that, despite its very low conductance, the density of ChR2 channels is high enough to produce large currents and reliably elicit action potentials in PCs of L7-ChR2 mice.

Next, the activation of PCs was characterized in vivo using juxtacellular recordings in anesthetized mice. Blue-light illumination was delivered through optical fibers coupled to a LED and positioned in the vicinity of the brain surface (*SI Methods* and Fig. 2*E*). In contrast to in vitro conditions, the irradiance received by the PCs in vivo depends strongly on the scattering of light in the tissue and varies as a function of the depth and orientation of the dendrite of the PC. PCs were identified by the occurrence of complex spikes (CSs), produced by the climbing-fiber input, and by the frequency of spontaneous simple spikes (mean CS rate = 0.44 ± 0.63 Hz; mean simple spike rate = 39.7 ± 3.9 Hz, $n = 19$, $n = 16$ mice). Increasing irradiance intensity led to an increase in simple spike firing rate in all cells ($n = 14$) whose somata lie in the first hundreds of micrometers from the surface of the tissue (Fig. 2 *F* and *G*). This increase in simple spike-firing rate could continue up to 500 ms (the longest duration tested) and reach up to 250 Hz. Further increasing the intensity induced a depolarization block consisting of a burst of spikes at light onset followed by a complete suppression of PC firing during the remaining time of illumination (Fig. 2*F*). Because of the diffusion of light (*SI Methods*; and see Fig. S5), depolarization block was not observed for cells distant from the tip of the optic fiber by more than 300 µm even at tip irradiance above 30 mW/mm$^2$. Also, no depolarization block was elicited with short pulses of light (≤2 ms). To quantify the onset of the effect of illumination, the latency of the first spike after the onset of illumination was measured. This latency was significantly shortened to a median delay of 5.5 ms ($n = 19$) (Fig. 2*H*) for irradiance as low as 2.5 mW/mm$^2$, and further decreased to a minimum median of 3.0 ms for an irradiance intensity of 19 mW/mm$^2$ (Fig. 2*H*). At the offset of the illumination, the time required to resume basal firing rate ranged between 10 and 30 ms (Fig. 2*I*). These findings demonstrate that ChR2-expressing PCs can be excited by light with high temporal precision in vivo.

**Inhibition of Cerebellar Nuclei Neurons by Purkinje Cells.** To assess whether the photostimulation of PCs was able to modulate the activity of their target neurons in the cerebellar nuclei (CN), in vivo extracellular recordings were performed with tetrodes in the CN while illuminating the ipsilateral cerebellar cortex (*SI Methods* and Fig. 3 *A* and *B*). To increase the probability of stimulating the group of PCs that target the recording site in the CN, we used illumination parameters that maximize the number of PCs excited (optical fiber of 600 µm diameter, 100-ms pulses, irradiance at 60 mW/mm$^2$) (*SI Methods*). Using these conditions, only 10% of activated PCs are likely to experience intensities that trigger a depolarization block (*SI Methods*; and see Fig. S5). By illuminating the lateral part of Crus I, sites that induced inhibition in recorded units from the interposed nucleus were found (26/48 tested sites; 21 animals) (Fig. 3 *C–G*). The suppression of firing was often accompanied by a small deflection in the field potential, presumably due to synaptic activation (red arrow, Fig. 3*C*). Usually, several cells were recorded simultaneously by the tetrode at each recording site (3.7 ± 1.7 cells per site) (Fig. 3*B*). Among the 97 cells recorded at responding sites (i.e., where at least one cell was inhibited), 70 cells were inhibited by Crus I illumination whereas 27 did not respond (average of 76 ± 26% inhibited cells at each site). These cells exhibited a mean firing rate of 18.0 ± 13.1 Hz and a coefficient of variation of 0.58 ± 0.29 for the interspike interval.

To quantify the effectiveness of the inhibition, the parameters of illumination were then varied (Fig. 3*E* and Fig. S3). Decreasing the intensity of irradiance to 19 mW/mm$^2$ did not change the proportion of responding cells at responding sites in the CN (72.8 ± 31% responding cells from 57 cells recorded at 25 responding sites in four mice), showing that this intensity is enough to recruit the minimum number of PCs necessary for CN inhibition. The duration of full inhibition (complete suppression of firing) increased with pulse duration and irradiance intensity (Fig. 3*E*). For 25-ms pulses, a complete inhibition of some CN units could be observed at irradiance higher than 3 mW/mm$^2$. The mean latency to full inhibition was slow but variable (mean = 18.9 ± 11.7 ms at 19 mW/mm$^2$ and 19.7 ± 12.15 ms at 60 mW/mm$^2$) (Fig. S3 *D–F*), which is consistent with the requirement of a large number of activated PCs for complete inhibition of CN firing. Finally, trains of 20-Hz and 30-Hz light pulses induced a rhythmic modulation of CN firing (Fig. S4). Taken together,

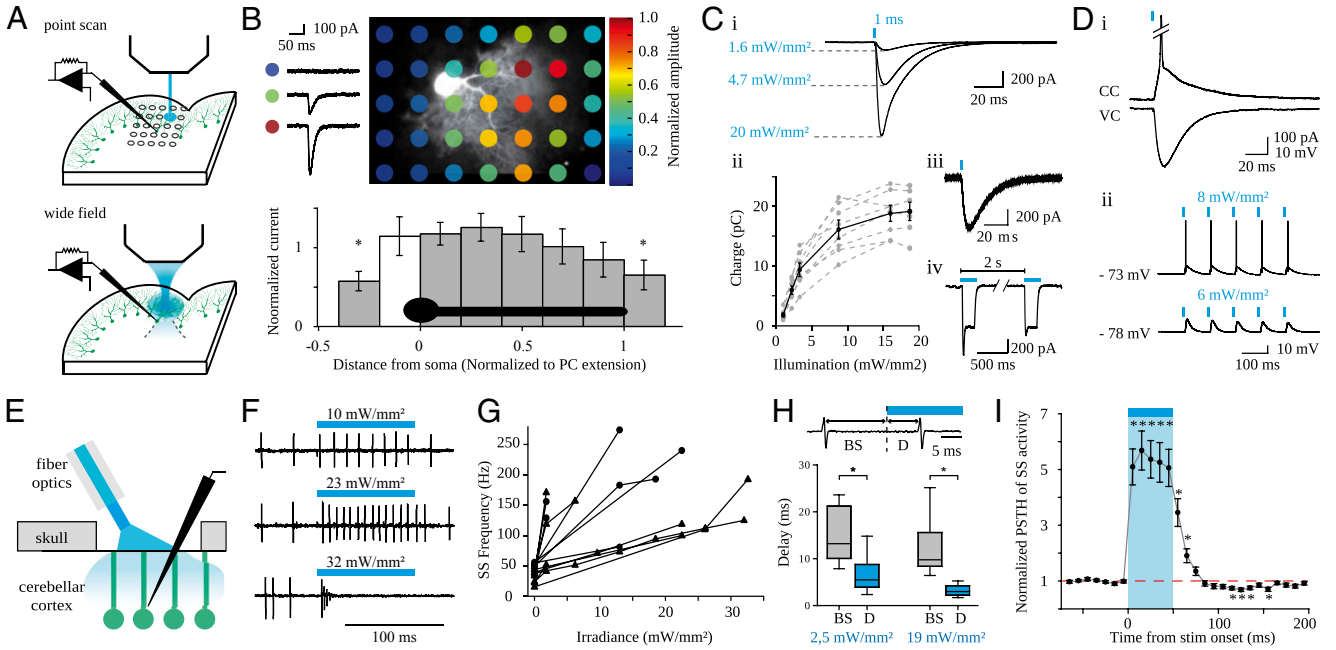


**Fig. 2.** Electrophysiological characterization of L7-ChR2(H134R)-eYFP mice in vitro and in vivo. (*A*) Schematics of acute cerebellar slices illustrating whole-cell recordings combined with laser-point scan photostimulation (*Upper*) or wide-field illumination (*Lower*). (*B, Upper*) Point-scan photostimulation (1-ms pulses) of Purkinje-cell dendrites and average current elicited at identified color-code points. (*Lower*) normalized current (± SEM) plotted against the distance from the soma ($n = 7$, Mann-Whitney test, $P < 0.05$). (*C, i*) Average whole-cell currents recorded in a PC with 1-ms wide-field LED illumination at various irradiances. (*ii*) Average charge against irradiance ($n = 8$ cells; black, mean ± SEM). (*iii*) Example of 10 successive traces superimposed from one cell. (*iv*) Desensitization of peak current at 0.5 Hz (100-ms pulses). Panels *iii* and *iv* are from different cells. (*D, i*) Action potential recorded in current-clamp mode elicited by a 1-ms light pulse (top) and corresponding photocurrent recorded in voltage clamp (bottom). (*ii*) Action potential initiation for burst of illumination (1-ms pulses at 10 Hz). (*E*) Schematic of in vivo juxtacellular recordings of PCs combined with optical fiber illumination. (*F*) Example traces recorded in juxtacellular mode during 100-ms pulses. (*G*) Relationship between PC firing rate and irradiance intensity ($n = 14$ cells). Triangle, cells deeper than 400 μm. (*H*) Delay of occurrence (D) of the first spike during illumination, compared with the preceding spike (BS) at various irradiances ($n = 20$ cells, 16 mice). Box plots show median values and 25/75% percentiles. Control median delay = 10.9 ms (quartiles: 8.4, 17.1); median delay = 5.5 ms (quartiles: 3.9, 8.8) at 2.5 mW/mm$^2$ and 3 ms (quartiles 2.2, 4.2) at 19 mW/mm$^2$, Kruskal–Wallis One-Way ANOVA, $P < 0.001$. Pairwise multiple comparison, Dunn's method, $^*P < 0.05$. Median delays during illumination were not significantly different. (*I*) Time course of the effect of illumination on the firing rate. Post stimulus time histograms (PSTHs) were normalized to the baseline frequency before averaging. Only cells with strong increases in firing rate (greater than twofold increase) were used in this panel. Kruskal–Wallis One-Way ANOVA, $P < 0.001$. Pairwise multiple comparisons, Dunn's method. $^*P < 0.05$.

these data show that illumination of PCs allows a dynamic control of CN firing (24) and that the duration of inhibition increases with the intensity and duration of light stimulations. Because PC inhibition has been proposed to produce a rebound excitation in CN neurons (25), we examined whether the instantaneous frequency was significantly enhanced relative to baseline values when the cells resumed their firing. The inhibition produced by PC inputs did not trigger a detectable rebound excitation even at high irradiance (60 mW/mm$^2$) in most CN cells (about 90%) but was followed by either a progressive or a direct return of CN discharge to its baseline value after the end of the stimulation (Fig. S3). To test the spatial specificity of the responses, the light source at the surface of the cerebellum was displaced from Crus I to Crus II, once a responding site was found; in most cells, the light-induced inhibition was lost ($n = 12/14$ cells recorded, six recording sites, four mice) (Fig. 3*F*), consistent with the zonal anatomical organization of the cortico-nuclear pathway. We then mapped the region of the CN inhibited by activation of ∼1000–3000 PCs in Crus I (pulse duration: 100 ms, irradiance 19 mW/mm$^2$; see Fig. 3*A*, Fig. S5, and *SI Methods*). The cellular responses were explored by systematic penetrations in ranges of stereotaxic coordinates [antero-posterior (AP) −5.9 to 6.4, medio-lateral (ML) 1.5; 2.5, depth 2.1, 3.3], and the most responsive sites were located in a small area (AP −6.2, −6.4, ML 1.7, 1.9, depth 2.7; 3.2) ($n = 106$ cells, 53 recording sites, four mice) (Fig. 3*G* and Fig. S3).

**Activation of Purkinje Cells Controls Inferior Olivary Neurons Discharge.** We then set out to assess whether the stimulation of a population of PCs can stop the firing of CN neurons and then influence the discharge of inferior olivary neurons. Complex spikes (CS) in PCs were monitored in juxtacellular recordings in vivo as a readout of olivary cells discharge. The recorded PC and its neighbors were then excited using small optical fibers (diameter 50–200 μm), and the irradiance was adjusted to obtain a strong activation without depolarization block (mean = 20.6 ± 11.7 mW/mm$^2$). Local illumination by pulses of light lasting 35–500 ms elicited a CS in 25 out of 42 PCs ($n = 25$ mice) (Fig. S6) with a mean latency of 138 ± 39 ms after the onset of the stimulation (Fig. 4 *A* and *B*). No response was observed for pulse durations of 10 and 20 ms. For pulse durations of 100 ms or less, most stimulation-induced CSs were elicited tens of milliseconds after the end of illumination, thus ruling out the possibility that CSs are a direct (artifactual) consequence of light stimulation. Indeed, no effect of illumination was detected in wild-type control mice either in PCs or in other cell types ($n = 4$ PCs, 7 non-PCs, presumably inhibitory interneurons from four wild-type mice). Interestingly, once a rebound CS was observed, the response rate was independent of the size of the fiber used ($F(1,23) = 2.85$, $P = 0.10$) and the irradiance at the tip of the optic fiber ($F(1,52) = 0.73$, $P = 0.40$). Therefore, data obtained using different irradiance intensities and fiber diameters were pooled together. No difference was observed in the onset of the CS responses for pulse durations between 35 and 500 ms whereas the offset of the response increased with pulse duration (Fig. 4*C*), suggesting that the beginning and the end of the

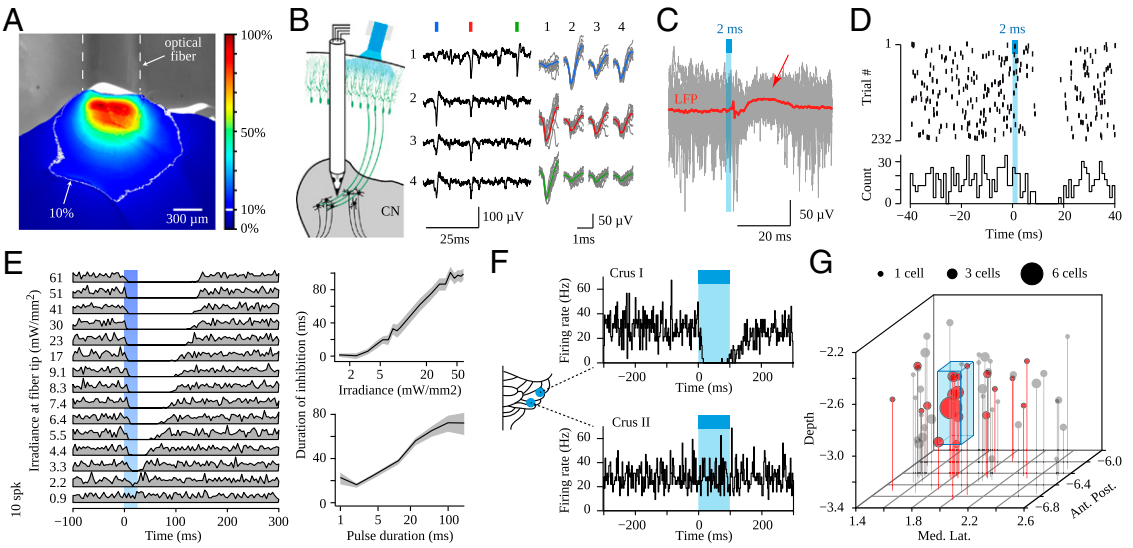


**Fig. 3.** Effective silencing of cerebellar nuclear cells by photostimulation of Purkinje cells in vivo. (*A*) Propagation of blue light in the cerebellar cortex (color coded part of the image) for a 600-µm optical fiber placed on the surface of the cerebellum (grayscale part of the image). In the color-coded part, the color of each pixel corresponds to its value expressed as a percentage of the intensity of the brightest pixel. The 10% isoline is delineated in white (i.e., corresponding to ~2 mW/mm$^2$ if the brightest pixel immediately under the fiber corresponds to 20 mW/mm$^2$). (*B*) Illustration of tetrode recordings in cerebellar nuclei. (*Left*) Schematics of the experiment. (*Center*) Example traces (vertical ticks of different colors signal different spikes; numbers identify the four channels of the tetrode). (*Right*) Average unfiltered waveforms on the four channels (same color code as for *Center*), superimposed on 10 successive events (gray traces). (*C*) Example of a recording obtained on one channel in the interposed nucleus. The average extracellular potential (LFP, local field potential, red) recorded in CN is superimposed on 30 successive sweeps (gray lines) aligned on the onset of photo-stimulation (2 ms, 60 mW/mm$^2$). Note the suppression of extracellular (negative) spikes after the stimulation. The average LFP was calculated from 232 sweeps. The red arrow signals the deflection of LFP. (*D*) Example of a raster plot (*Upper*) and corresponding PSTH (*Lower*; bin, 1 ms), showing a complete suppression of firing following the stimulation (blue bar); the example is the same as in *C*. (E, *Left*) Example of PSTHs for one cell tested with different light intensities (pulse duration, 25 ms). (*Right*) Average duration of full inhibition plotted against the irradiance at the fiber tip (at 25 ms) or pulse duration (at 60 mW/mm$^2$) ($n = 74$ cells) (*SI Methods*). The shaded area indicates the SEM. (*F*) Example cell inhibited in response to the illumination of Crus I (*Upper*, PSTH), but not Crus II (*Lower*, PSTH). Bin, 5 ms. Blue bar, light pulse (100 ms, 60 mW/mm$^2$). (*G*) A 3D view of the distribution of CN recording sites where inhibited cells were found (red) or not (gray) during Crus I illumination (100 ms, 19 mW/mm$^2$) on the ipsilateral cerebellar Crus I region (AP, −6.1; ML, 3.3). The 3D rectangle arrow identifies the region where most responsive sites are clustered. See Fig. S3 planar projections.

response are locked respectively to the beginning—with a long delay—and to the end of the stimulation. Therefore, CS were evoked by pulses of irradiance around 20 mW/mm$^2$ using a 100-µm optical fiber that should activate about 200–500 PCs (Fig. 4*A* and Fig. S5). Taken together, these results indicate that, provided a critical number of PCs were illuminated for a minimal period (35 ms), the disinhibition of olivary neurons resulted in CSs evoked with a minimal delay of 80–100 ms. Moreover, experiments in which the optical fiber was moved along the transverse axis above the surface showed that the evoked CS response (i.e., the inferior olive disinhibition) decreased and disappeared together with the simple spike response (i.e., the direct activation of the recorded cell) (Fig. 4*E*). These results indicate that the set of PCs that control the climbing fiber afferent to a PC is localized close to that PC (Fig. 4*F*), consistent with the topographical organization of the cortico-nucleo-olivary circuit.

There is a substantial jitter in the time of occurrence of the CS after the onset of illumination (several tens of milliseconds) (Fig. 4 *B* and *D*), suggesting a temporal fluctuation of the responsiveness of the inferior olivary neurons to disinhibition. There was indeed a correlation between the probability of occurrence of the CS following the stimulation of PCs and the CS baseline firing rate (Fig. S6*B*), indicating that PC illumination is more efficient when olivary cells are more depolarized. Because inferior olivary neurons are known to express subthreshold oscillations spontaneously (26), we examined whether such oscillations would condition the timing of the CS evoked by PCs stimulations. Poststimulus time histograms were constructed by aligning individual trials on the time of the first CS after the onset of stimulation (Fig. 4*D*, green ticks; 100 ms pulse, $n = 8$), and the evoked CS were found to occur preferentially ~225 ms and ~450 ms after a preceding spontaneous CS (Fig. 4*D*, *Bottom*). These results show that the disinhibition of olivary neurons triggers CS spikes in phase with an ~4-Hz subthreshold oscillation.

## Discussion

In this study, a transgenic mouse line expressing ChR2 specifically in PCs is described and used to investigate the functional organization of the olivo-cerebellar circuit. The level of ChR2 (H134) expression yielded reliable and sustained currents (23, 27) in PCs and increased the cells' discharge. Focal illumination in one specific part of the cerebellar cortex (crus I) transiently inhibited 75% of the cells recorded simultaneously from the same tetrode in a restricted area of the cerebellar nuclei. Lowering the intensity of stimulation did not change the percentage of responsive cells at responsive sites, suggesting that the non-responsive cells receive weaker PC inputs, as it has been suggested for nuclear GABAergic interneurons (28). Although light stimulations took a few milliseconds to evoke spikes in PCs, the complete suppression of firing in CN cells was variable among cells and was reached on average in ~20 ms, indicating the need for a high convergence of presynaptic PCs or a temporal summation of inhibitory PC inputs to fully inhibit CN neurons. Surprisingly, although sustained inhibition was induced in CN neurons following activation of PCs, rebound excitation (29, 30) was observed in only ~10% of the cells, in agreement with the study of Alviña et al. (31). Anesthesia might alter physiological properties of CN neurons. However, recent studies (25, 32) have demonstrated that rebound excitation in CN neurons requires the extensive activation of the presynaptic PCs. Thus, a more likely interpretation is that our protocol of illumination leads to poorly synchronized PC discharges and/or fails to recruit enough presynaptic PCs.

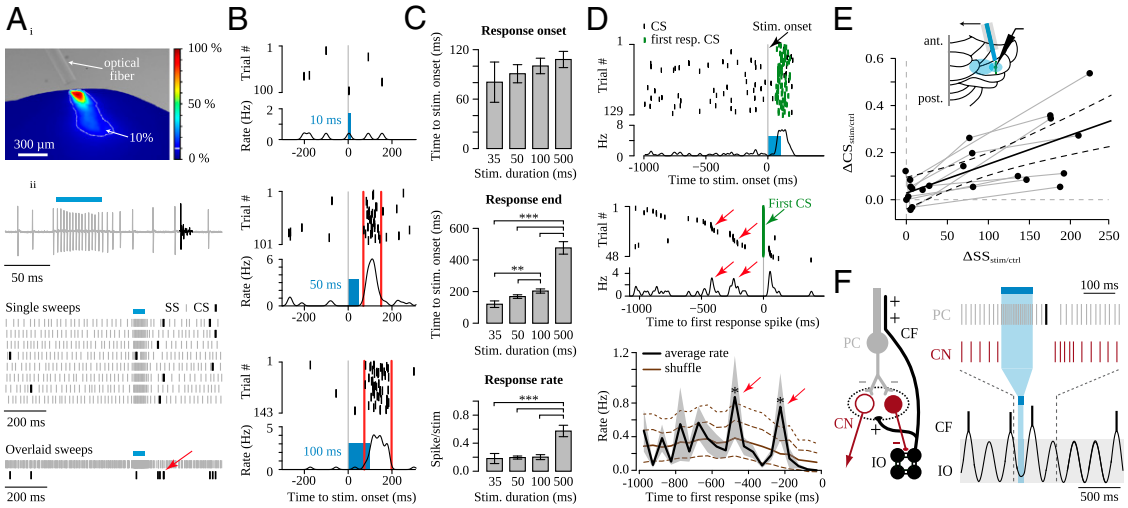


**Fig. 4.** Photostimulation of Purkinje cells controls inferior olivary cell discharge. (*A*, *i*) Blue–light propagation observed in a transverse section of the cerebellar cortex using a 100-µm optical fiber. The same code as in Fig. 3*A*. (*ii*) Individual trace from in vivo juxtacellular PC recordings and corresponding raster plot for both simple spikes (gray ticks) and CSs (black ticks, the signature of olivary cell discharge in PCs). Light illumination elicited CSs in the recorded PC. The arrow indicates the evoked complex spikes. (*B*) Example raster plot and average peri-stimulation firing rate (obtained from the density of spikes convolved with a Gaussian kernel with a 10-ms variance) of CSs recorded with 10-, 50-, and 100-ms illumination pulses (blue rectangles). Red lines identify the time periods with significant increase in the CS firing rate relative to baseline. (*C*) Mean latency from stimulation onset to response onset (*Top*, no significant difference, $F_{1,56} = 0.074$, $P = 0.79$) and response end (*Middle*, significant difference across conditions, $F_{1,56} = 465$, $P < 10^{-4}$), and mean response rate (spike/stim, *Bottom*, significant difference across conditions, $F_{1,56} = 56$, $P < 10^{-4}$) for 35-, 50-, 100-, and 500-ms pulses ($n = 4$, 13, 19, and 11 cells, respectively; 50–200 trials by conditions). *, **, ***$P < 0.05$, 0.01, and 0.001, respectively. (*D*) Influence of the recent history of CS firing on the timing of the disinhibitory response. For each cell, the PSTH (*Top*) was recalculated to realign the trials on the time of the first CS after stimulus onset (*Middle*, green CSs are aligned, trials without CS are not represented). In the example (*Middle*), the trials are sorted by decreasing ISIs before the response CS showing that the first response spikes occurred preferentially after specific ISIs (red arrows); in some trials, the illumination triggered two CSs yielding a peak at positive times. The realigned PSTH were averaged for eight cells (*Bottom*) and compared with the expected values after randomly shifting the preresponse CS (±300 ms). The disinhibitory response occurred preferentially after specific intervals (*) after the last prestimulation CS spikes. Dashed and dotted lines represent shuffled PSTH ± 1 SD and 2 SD respectively. (*E*) Increase of CS frequency against the modulation of simple spike frequency after blue-light illumination at different optical-fiber position. Points acquired from the same cell are connected by a gray line. A linear fit (black line, $r^2 = 0.7$) with confidence interval at 95% (dashed black line) is superimposed on the data showing the correlation between direct PC activation and CS response (and the simultaneous disappearance of both responses when the fiber is moved away). (*F*) Diagram of the synaptic connections in the olivo-cortico-nucleo-olivary loop and illustration of discharge in Purkinje cells, CN neurons, and olivary cells based on our results. Blue light activates PCs (simple spike firing rate increased during stimulation, gray ticks) that stop CN neuron discharge and consequently disinhibit inferior olive neurons. A CS is then observed in PCs. Ticks illustrate neuronal discharge.

The stimulation of PCs during tens of milliseconds elicited olivary discharge with an onset latency close to 100 ms and an offset latency that increased with stimulation duration. Such long-latency phenomenon has been previously suggested in behaving monkeys (33) by analyzing the simple spike discharge preceding complex spikes. In our experiments, the CS response started while the CN neurons were still inhibited, which rules out the recruitment of an (indirect) excitatory output of the CN to the inferior olive (15, 34). However, the evoked CS is consistent with properties of the nucleo-olivary inhibitory pathway (35), which is dominated by asynchronous release (17) leading to long latencies for inhibition (18); this mode of transmission should delay the transmission of changes in CN firing rate and filter out very transient suppressions of CN firing. Moreover, the variability of the latency of the CS response across trials seems to be partly due to intrinsic subthreshold fluctuations (26) (in our case, 4-Hz oscillation) of the membrane potential of inferior olivary neurons. Indeed, the maximal probability of occurrence of CS response was found in phase with olivary oscillations. Overall, the characteristics of the CS response to increased PC discharge are consistent with a disinhibition of the inferior olive via the nucleo-olivary pathway. Our results are also consistent with a topographical organization of the cortico-nucleo-olivary pathway. CN neurons inhibition was lost when the illumination was moved to a neighboring lobule. Moreover, the CS response in the recorded PCs disappeared as soon as direct excitation (evidenced by simple spike modulation) was lost when the optic fiber was moved away in the transverse direction. The combination of these results and those from previous studies (9, 16, 24, 26, 27, 30–32, 36) strongly argue for the existence of closed cortico-nucleo-olivary loops where spatially restricted sets of PCs control their afferent climbing fibers. The spatial extension of the set of PCs excited by our smallest illumination (around 300 µm diameter) is closer to the scale of cerebellar zones than of microzones (11). Indeed, recent imaging studies in vivo describing synchronized CSs during sensory stimulation identified microbands narrower than 100 µm (37, 38). Testing whether the control of the CS is segregated across such microzones may require the use of specific strategies (39) to restrict the expression of the opsin to single microzones and therefore circumvent the difficulty of illuminating very narrow bands of cells. The closed cortico-nucleo-olivary loops will favor the triggering of a CS volley in a subset of PCs shortly after their firing rate is increased. Moreover, because the nucleo-olivary inhibitory pathway targets gap junctions between olivary cells and promotes their decoupling (7, 40), the inhibition of this pathway should promote CS synchrony (19, 41). This feedback excitatory loop could also modulate plasticity in the cerebellar cortex, for example, at the parallel fiber to PC synapse because the delay between the onset of the increased PCs firing and the rebound CS (around 100 ms) matches the optimal interval between parallel-fiber and climbing-fiber discharges required for the induction of long-term depression (42, 43). Indeed, the nucleo-olivary pathway has been proposed to play important roles in conditioning (44, 45), and an appealing possibility is that the cortico-nuclear pathway controls the contribution of the nucleo-olivary pathway to motor learning. A wide range of theoretical and experimental evidence has led to the proposal that learning mechanisms in the cerebellar cortex

underlie the formation and the storage of internal models of the sensory-motor system (46). These models convert desired movements into motor commands or predict sensory outcomes of planned movements (47); the adjustment of the models is performed by supervised learning via the climbing fibers. The cortico-nucleo-olivary pathway described in our study provides a way to propagate the predictions computed in the cerebellar cortex to the inferior olive, where it can be compared, with an appropriate delay, with the actual outcome of the ongoing task carried by other inputs to the inferior olive. Therefore, the closed cortico-nucleo-olivary loops may play an essential role in adjusting the internal models in the cerebellum.

## Methods

All experimental procedures conform to Centre National de la Recherche Scientifique and National Institutes of Health guidelines on animal experimentation. A BAC transgenic mouse expressing channelrhodopsin-2(H134R) under the control of the regulatory elements of the L7-pcp2 gene was generated (21) (*SI Methods* and Fig. S1). In vivo extracellular recordings of PCs were performed in anesthetized animals (*SI Methods*). Means were given ± SD unless otherwise stated.

**ACKNOWLEDGMENTS.** We thank Pr Karl Deisseroth for kindly providing the pAAV-double floxed-hChR2(H134R)EYFP-WPRE-pA vector. We thank the Mouse Clinical Institute, Laurence Huck, and Cassidy Fiford for technical assistance. We thank Samuel Garcia for support on software and Boris Barbour and Nancy Grant for comments on this manuscript. This work was supported by the Centre National pour la Recherche Scientifique, Ecole Normale Supérieure, Institut National de la Santé et de la Recherche Médicale, Université de Strasbourg, Ministère de la Recherche, Agence Nationale pour la Recherche Grants ANR-09-MNPS-038 CeCoMod, ANR-2010-JCJC-1403-1 MicroCer, and ANR-GUI-AAP-04 Sensocode; the INTERREG IV Rhin Supérieur Program; and the European Funds for Regional Development, TIGER project. Publication costs are supported by the Neurex network (www.neurex.org).

1. Ito M (2006) Cerebellar circuitry as a neuronal machine. *Prog Neurobiol* 78(3-5):272–303.
2. Thach WT, Goodkin HP, Keating JG (1992) The cerebellum and the adaptive coordination of movement. *Annu Rev Neurosci* 15:403–442.
3. Dean P, Porrill J, Ekerot C-F, Jörntell H (2010) The cerebellar microcircuit as an adaptive filter: Experimental and computational evidence. *Nat Rev Neurosci* 11(1): 30–43.
4. Ito M (1984) *The Cerebellum and Neural Control* (Raven, New York).
5. De Zeeuw CI, et al. (2011) Spatiotemporal firing patterns in the cerebellum. *Nat Rev Neurosci* 12(6):327–344.
6. Llinás RR (2011) Cerebellar motor learning versus cerebellar motor timing: The climbing fibre story. *J Physiol* 589(Pt 14):3423–3432.
7. Yarom Y, Cohen D (2002) The olivocerebellar system as a generator of temporal patterns. *Ann N Y Acad Sci* 978:122–134.
8. Barmack NH (2006) Inferior olive and oculomotor system. *Prog Brain Res* 151:269–291.
9. Oscarsson O (1979) Functional units of the cerebellum—sagittal zones and microzones. *Trends Neurosci* 2:143–145.
10. Voogd J, Glickstein M (1998) The anatomy of the cerebellum. *Trends Neurosci* 21(9): 370–375.
11. Apps R, Hawkes R (2009) Cerebellar cortical organization: A one-map hypothesis. *Nat Rev Neurosci* 10(9):670–681.
12. Glickstein M, Sultan F, Voogd J (2011) Functional localization in the cerebellum. *Cortex* 47(1):59–80.
13. Nelson BJ, Adams JC, Barmack NH, Mugnaini E (1989) Comparative study of glutamate decarboxylase immunoreactive boutons in the mammalian inferior olive. *J Comp Neurol* 286(4):514–539.
14. Teune TM, van der Burg J, de Zeeuw CI, Voogd J, Ruigrok TJ (1998) Single Purkinje cell can innervate multiple classes of projection neurons in the cerebellar nuclei of the rat: A light microscopic and ultrastructural triple-tracer study in the rat. *J Comp Neurol* 392(2):164–178.
15. Teune TM, van der Burg J, van der Moer J, Voogd J, Ruigrok TJ (2000) Topography of cerebellar nuclear projections to the brain stem in the rat. *Prog Brain Res* 124: 141–172.
16. Bengtsson F, Hesslow G (2006) Cerebellar control of the inferior olive. *Cerebellum* 5(1):7–14.
17. Best AR, Regehr WG (2009) Inhibitory regulation of electrically coupled neurons in the inferior olive is mediated by asynchronous release of GABA. *Neuron* 62(4): 555–565.
18. Bazzigaluppi P, Ruigrok T, Saisan P, De Zeeuw CI, de Jeu M (2012) Properties of the nucleo-olivary pathway: An in vivo whole-cell patch clamp study. *PLoS ONE* 7(9): e46360.
19. Marshall SP, Lang EJ (2009) Local changes in the excitability of the cerebellar cortex produce spatially restricted changes in complex spike synchrony. *J Neurosci* 29(45): 14352–14362.
20. Chen X, et al. (2010) Disruption of the olivo-cerebellar circuit by Purkinje neuron-specific ablation of BK channels. *Proc Natl Acad Sci USA* 107(27):12323–12328.
21. Gong S, et al. (2003) A gene expression atlas of the central nervous system based on bacterial artificial chromosomes. *Nature* 425(6961):917–925.
22. Lin JY (2011) A user's guide to channelrhodopsin variants: Features, limitations and future developments. *Exp Physiol* 96(1):19–25.
23. Berndt A, et al. (2011) High-efficiency channelrhodopsins for fast neuronal stimulation at low light levels. *Proc Natl Acad Sci USA* 108(18):7595–7600.
24. Person AL, Raman IM (2012) Purkinje neuron synchrony elicits time-locked spiking in the cerebellar nuclei. *Nature* 481(7382):502–505.
25. Bengtsson F, Ekerot CF, Jörntell H (2011) In vivo analysis of inhibitory synaptic inputs and rebounds in deep cerebellar nuclear neurons. *PLoS ONE* 6(4):e18822.
26. Khosrovani S, Van Der Giessen RS, De Zeeuw CI, De Jeu MT (2007) In vivo mouse inferior olive neurons exhibit heterogeneous subthreshold oscillations and spiking patterns. *Proc Natl Acad Sci USA* 104(40):15911–15916.
27. Zhao S, et al. (2011) Cell type–specific channelrhodopsin-2 transgenic mice for optogenetic dissection of neural circuitry function. *Nat Methods* 8(9):745–752.
28. Uusisaari M, Knöpfel T (2011) Functional classification of neurons in the mouse lateral cerebellar nuclei. *Cerebellum* 10(4):637–646.
29. Tadayonnejad R, et al. (2010) Rebound discharge in deep cerebellar nuclear neurons in vitro. *Cerebellum* 9(3):352–374.
30. Aizenman CD, Linden DJ (1999) Regulation of the rebound depolarization and spontaneous firing patterns of deep nuclear neurons in slices of rat cerebellum. *J Neurophysiol* 82(4):1697–1709.
31. Alviña K, Walter JT, Kohn A, Ellis-Davies G, Khodakhah K (2008) Questioning the role of rebound firing in the cerebellum. *Nat Neurosci* 11(11):1256–1258.
32. Hoebeek FE, Witter L, Ruigrok TJ, De Zeeuw CI (2010) Differential olivo-cerebellar cortical control of rebound activity in the cerebellar nuclei. *Proc Natl Acad Sci USA* 107(18):8410–8415.
33. Miall RC, Keating JG, Malkmus M, Thach WT (1998) Simple spike activity predicts occurrence of complex spikes in cerebellar Purkinje cells. *Nat Neurosci* 1(1):13–15.
34. Ruigrok TJ, de Zeeuw CI, van der Burg J, Voogd J (1990) Intracellular labeling of neurons in the medial accessory olive of the cat. I. Physiology and light microscopy. *J Comp Neurol* 300(4):462–477.
35. Lang EJ, Sugihara I, Llinás R (1996) GABAergic modulation of complex spike activity by the cerebellar nucleoolivary pathway in rat. *J Neurophysiol* 76(1):255–275.
36. Sugihara I, et al. (2009) Projection of reconstructed single Purkinje cell axons in relation to the cortical and nuclear aldolase C compartments of the rat cerebellum. *J Comp Neurol* 512(2):282–304.
37. Ozden I, Sullivan MR, Lee HM, Wang SS (2009) Reliable coding emerges from coactivation of climbing fibers in microbands of cerebellar Purkinje neurons. *J Neurosci* 29(34):10463–10473.
38. Ghosh KK, et al. (2011) Miniaturized integration of a fluorescence microscope. *Nat Methods* 8(10):871–878.
39. Tsubota T, Ohashi Y, Tamura K (2013) Optogenetics in the cerebellum: Purkinje cell-specific approaches for understanding local cerebellar functions. *Behav Brain Res*, 10.1016/j.bbr.2013.04.019.
40. de Zeeuw CI, Holstege JC, Ruigrok TJ, Voogd J (1989) Ultrastructural study of the GABAergic, cerebellar, and mesodiencephalic innervation of the cat medial accessory olive: Anterograde tracing combined with immunocytochemistry. *J Comp Neurol* 284(1):12–35.
41. Welsh JP, Llinás R (1997) Some organizing principles for the control of movement based on olivocerebellar physiology. *Prog Brain Res* 114:449–461.
42. Safo P, Regehr WG (2008) Timing dependence of the induction of cerebellar LTD. *Neuropharmacology* 54(1):213–218.
43. Wang SS, Denk W, Häusser M (2000) Coincidence detection in single dendritic spines mediated by calcium release. *Nat Neurosci* 3(12):1266–1273.
44. Rasmussen A, Jirenhed DA, Hesslow G (2008) Simple and complex spike firing patterns in Purkinje cells during classical conditioning. *Cerebellum* 7(4): 563–566.
45. Kim JJ, Krupa DJ, Thompson RF (1998) Inhibitory cerebello-olivary projections and blocking effect in classical conditioning. *Science* 279(5350):570–573.
46. Ito M (2008) Control of mental activities by internal models in the cerebellum. *Nat Rev Neurosci* 9(4):304–313.
47. Kawato M (1999) Internal models for motor control and trajectory planning. *Curr Opin Neurobiol* 9(6):718–727.

# Supporting Information

## Chaumont et al. 10.1073/pnas.1302310110

### SI Methods

**BAC Modification and Transgenic Mice.** A 1-kb homology box located 5′ of the ATG of the *pcp2* gene was amplified by PCR from bacterial artificial chromosome (BAC) RP24-186D18 and subcloned in the pLD53.SC2 shuttle vector. The cDNA encoding hChR2(H134R)EYFP was amplified from the vector pAAV-double floxed-hChR2(H134R)EYFP-WPRE-pA (kindly provided by K. Deisseroth, Stanford University, Standford, California), and placed behind the pcp2 homology box. The resulting pcp2/hChR2(H134R)EYFP shuttle vector was used to modify the BAC RP24-186D18 by homologous recombination according to previously published protocols (1). The recombination design allows the replacement of the pcp2 ATG by the cDNA construct in the BAC, effectively placing the expression of the channelrhodopsin hChR2(H134R)EYFP construct under the control of the regulatory elements of the pcp2 gene. Correct modification of the RP24-186D18 BAC was visualized by Southern blot on BAC DNA digested by EcoRI, separated on 0.8% agarose gel, and probed with digoxigenin-labeled pcp2 homology box. Pulsed-field gel electrophoresis was performed on BAC DNA digested by SpeI. A correctly modified BAC was selected (Fig. 1*A*) based on the pattern observed by Southern blot and pulsed-field gel analysis (including no visible reorganization of the BAC). This BAC was amplified and purified using a cesium chloride gradient. DNA was then dialyzed in oocyte injection buffer for generation of transgenic mice (injection performed by the Institut Clinique de la Souris, Illkirch, France). Founders were genotyped using two sets of primers ensuring the integrity of the inserted BAC: one set in the BAC backbone (forward: 5′GTGATATCGCGGAAGGAAAA3′; reverse: 5′AGGATATACGGCAGGCATTG3′), another set encompassing the L7 homology box and the ChR2 cDNA (forward: 5′GCTTCTTCAACCTGCTGACC3′; reverse: 5′aaaaatgtgttcgcgccata3′).

**In Vitro Recordings.** All experimental procedures conformed to Centre National de la Recherche Scientifique and National Institutes of Health guidelines on animal experimentation. Slices were prepared from juvenile L7-ChR2-eYFP mice (postnatal 15 to 24) as described in ref. 2. Following anesthesia by isoflurane inhalation, animals were killed by decapitation, the cerebellum was dissected out and placed in a cold artificial cerebrospinal fluid (ACSF) (4 °C) bubbled with carbogen [95% $O_2$, 5% $CO_2$ (vol/vol)], containing in mM: NaCl 120; KCl 3; $NaHCO_3$ 26; $NaH_2PO_4$ 1.25; $CaCl_2$ 2.5; $MgCl_2$ 2. Glucose 10, Minocyclin 0.00005 (Sigma-Aldrich). The 330 μm-thick sagittal slices were prepared (Microm HM 650V, Microm) in potassium-based medium, containing in mM: K-gluconate 130; KCl 14.6; EGTA 2; Hepes 20; Glucose 25; minocyclin 0.00005, and D-AP5 0.05. This method was used to protect acute brain slices during cutting (3). After cutting, slices were soaked a few seconds in a sucrose-based medium at 34 °C, containing in mM: sucrose 230; KCl 2.5; $NaHCO_3$ 26; $NaH_2PO_4$ 1.25; glucose 25; $CaCl_2$ 0.8; $MgCl_2$ 8; minocyclin 0.00005; and D-APV 0.05. Slices were maintained in a water bath at 34 °C in bubbled ACSF. Experiments were done at 34 °C using the same bubbled ACSF. Drugs were obtained from Tocris-Cookson or Ascent Scientific. Purkinje cells (PCs) were whole-cell patch-clamped both in voltage and current clamp mode using 3- to 4-MΩ pipettes with a Multiclamp 700 amplifier (Molecular Devices), and optimal series resistance ($R_s$) compensation (80% of 5–10 MΩ typically) was applied. $R_s$ was monitored in all experiments, and cells were held at −60 mV (Figs. 1 and 2) or −70 mV (Fig. S2). The pipette solution contained (in mM): $KMeSO_4$ 135; NaCl 6, Hepes 10; MgATP 4; $Na_2GTP$ 0.4, with pH adjusted to 7.3 with KOH and osmolarity to 300 mOsm. Voltages were not corrected for the liquid junction potential, which was calculated to be 9 mV (i.e., the real membrane potential was 9 mV more hyperpolarized than reported). Currents in Purkinje cells were low-pass filtered at 2 kHz, and then sampled at 20-50 kHz. Acquisition of data and control of light illumination were performed using the WinWCP 4.2.x freeware (John Dempster, University of Strathclyde, Glasgow, UK).

**In Vitro Photostimulation.** For experiments of Fig. 2 *C* and *D*, PCs were photostimulated using wide field LED-based illumination (collimated LED M470L2-C1 powered by a T-cube LEDD1B driver from Thorlabs or a collimated black LED 460 nm from Prizmatix) through the objective (20×, NA = 0.5) of the microscope (BX51 Olympus). Irradiance was measured with a PM100D power meter equipped with an S120C photodiode sensor (Thorlabs) under the objective, and the illuminated area was estimated to a disk of 600 μm. In Fig. 2*B*, a 473-nm diode-pumped solid-state (DPSS) laser (CrystaLaser) was used for laser scan illumination on an Olympus microscope. In Fig. S2, photostimulation at 460nm (Lumen Dynamics X-cite XLED1) was carried out on an optogenetic workstation based on a Leica DM6000 FS fixed-stage microscope, with patterned illumination (digital micromirror device; AndorTM Mosaic). The position and shape of illumination masks were verified by using a mirror slide straight after the experiment. The homogeneous illumination over masks of defined size enabled the accurate calibration of the irradiance. Recorded PCs were loaded with alexa 568 to draw the masks and estimate their depth (on average ∼30 μm below the slice surface).

**Surgery.** Mice were anesthetized using urethane (1.9 g/kg i.p.) and mounted in a stereotaxic frame (Model 942; David Kopf Instruments; or SR-6M; Narishige). Their body temperature was maintained at 36–37 °C throughout the experiment using a heating blanket controlled by rectal temperature (CMA 450, CMA or TC-1000; CWE Inc). Before scalp incision, 3% lidocaine was injected s.c. at the incision site. After incision, the skull was exposed, and a craniotomy was drilled above the right cerebellar hemisphere. During surgery, a long pass filter (cut on 550 nm) on white-light apparatus was used to avoid spurious ChR2 activation. The surface of the cerebellum was kept moist with a saline solution throughout the experiment. For juxtacellular recordings, mice were ventilated (SAR-830/P, BIOSEB; Dwyer). All in vivo electrophysiological experiments were performed on anesthetized mice.

**Rotarod.** To evaluate motor coordination, mice were placed on immobile rotarod cylinders, which ramped up from 0 to 45 rotations per minute (IITC) in 180 s. The timer was stopped when the mouse fell off the cylinder or did a whole turn with it. For a given session, this procedure was repeated three consecutive times. The full experiment comprised three sessions per animal, separated by 90 min.

**in Vivo Juxtacellular Recordings and Data Analysis.** Juxtacellular recordings in anesthetized mice were made as in ref. 4 using 15–30 MΩ resistance borosilicate glass pipettes (Warner Instruments), filled with a 0.5 M NaCl solution and mounted on motorized micromanipulators (Luigs and Neumann). Data were recorded and filtered between 300 Hz and 5 kHz and sampled at 20 kHz using an amplifier in current clamp mode (ELC 03XS; NPI). Acquisition of data and control of light illumination were

performed using the WinWCP 4.2.x freeware (John Dempster). Spike sorting and data storage were designed with OpenElectrophy open source software in a sql environment (http://neuralensemble.org/OpenElectrophy/) [Garcia and Fourcaud-Trocmé (5)].

**Cerebellar Nuclei Recordings.** For electrophysiological recordings, a commercial quartz tetrode (Thomas Recordings) was lowered into the right nucleus interpositus (from Bregma, −6.2 to −6.4 mm antero-posterior (AP), 1.5–2.0 mm medio-lateral (ML), and 2.4–2.8 mm below brain surface). As we showed earlier, these tetrodes produce more reliable penetrations of the cerebellar cortex and less tissue damage than conventional wire tetrodes (6). Each tetrode was covered with dye (Vybrant DiI; Life Technologies), and its position in the nucleus interpositus was verified by post hoc analysis of cryostat brain sections. Extracellular potentials measured by the tetrode were amplified and digitized using a System 3 workstation purchased from Tucker Davis Technologies.

**In Vivo Photostimulation of Purkinje Cells.** Light was delivered to discrete areas of the exposed cerebellar surface using a high-brightness blue light emitting diode (LED) coupled with optical fibers of different diameters (50, 100, 200, and 600 μm, numerical aperture 0.22, 0.22, 0.48, and 0.37), purchased from Prizmatix or Doric Lenses. The LED had a peak wavelength of 460 or 463 nm and a spectral bandwidth (full-width at half maximum) of 27 or 24 nm. Light pulses were generated using a universal LED controller (Prizmatix; SLC-AA02-US; Mightex Systems) triggered from the electrophysiology acquisition software (WinWCP or Tucker-Davis). Optical power at the fiber tip was measured with a PM100D power meter equipped with an S120C photodiode sensor (Thorlabs). The waveform and timing of individual light pulses were monitored using a silicon photodiode (SM1PD1A; Thorlabs). All values of irradiance in the text correspond to the value at the tip of the optic fiber. For photostimulation of Purkinje cells, the tip of the optical fiber was positioned in close vicinity or in contact with the cerebellar surface (except in the experiments where the fiber was moved while recording the cell).

Initially, a 200-μm fiber was used to study Purkinje-cell response to blue light in juxtacellular recordings and control the emission of spikes by olivary cells as shown in Fig. 4. In an attempt to restrict the spread of light, a set of experiments with a fiber of 100 μm diameter (and a few experiments using a fiber of 50 μm) was performed. In these experiments, the irradiance at the tip of the optical fiber was adjusted to compensate for light diffusion between the optical fiber and the recorded PC (and its neighbors), so that it generated a strong increase in the frequency of simple spikes but remained below the threshold triggering depolarization block in the recorded PC.

A 600-μm-diameter fiber combined with high irradiance was used for the recordings in the cerebellar nuclei: in these experiments we needed to stimulate a larger area to increase the chance to stimulate the few tens of Purkinje cells that contact the cerebellar nuclei (CN) units recorded.

In the experiment of Fig. 4*E* for which the fiber was moved while recording the PC, the fiber had to be kept distant from the surface to avoid the loss of the cell, thus yielding more diffuse activation [these data were analyzed by comparing the occurrence of the light-evoked complex-spike (CS) response to the modulation of the simple-spike discharge as a signature of a direct effect].

**Estimation of the Number of Stimulated Purkinje Cells.** To estimate the number of cells activated during photostimulation, we first assessed the volume of tissue that received enough light to increase the simple spike firing rate and then calculated the number of Purkinje cells in this volume.

We first performed a series of experiments as in ref. 7 using freshly dissected hemisectioned cerebellum maintained in saline and embedded in 2% agarose gel to hold the surface horizontal. An opening in the agarose gel surrounding the tissue was made around CrusII to bring an optical fiber next to the cerebellar surface. The optical fibers (100 μm core 0.22 NA and 600 μm core 0.37 NA) were positioned against the *pia* in a plane parallel to the section and with a distance and angle relative to the surface as in the in vivo CN recordings (Fig. 3) and evoked CS experiments (Fig. 4 *A–D*). The cut surface was imaged from the top using a CCD camera; this measure provides a coarse estimate of the power density distribution in the depth of the cerebellar cortex. Series of images were collected while the optical fiber was translated vertically to change the distance between the axis of the fiber and the plane of the section (Fig. S5), thus exploring the lateral extension of the power density profiles.

We then estimated the volume receiving enough light to activate Purkinje cells (i.e., irradiances $\geq$ 2 mW/mm$^2$) in experiments aimed at studying the nuclear and olivary responses (Figs. 3*A* and 4*A*). For irradiance of 20 mW/mm$^2$ at the fiber tip (intensity used for mapping the CN responsive area and mean intensity in the study of olivary disinhibition), we identified on all images the pixels with intensities above 10% of the intensity of the brightest pixel immediately underneath the fiber. (This provides probably an overestimation of the volume because, for this brightest pixel, the irradiance is probably lower than the irradiance at the fiber tip, and thus the 10% threshold corresponds to an even lower irradiance threshold.) For the 100-μm fiber, this volume has a roughly conical shape, with a maximal width of 360 μm in the transverse direction and 800 μm in the sagittal direction. For the 600-μm fiber, we found a roughly spherical volume with a diameter of 1,300 μm. Purkinje cells are organized in layers that are intersecting these volumes. For planar layers, this intersection will have an elliptic surface of at most 0.2 mm$^2$ for the 100-μm fiber, and a circular surface of at most 1.3 mm$^2$ for the 600-μm fiber. In the mouse, the total surface of the Purkinje-cell layer has been estimated to ∼190 mm$^2$ (8) or 80 mm$^2$ (9). According to these authors, the patch of activated Purkinje cells will represent 0.1–0.25% (respectively 0.7–1.6%) of the total Purkinje-cell layer surface when using a 100-μm (respectively 600 μm) optical fiber. Using a density of Purkinje cell of 1,018 per mm$^2$ [Napper and Harvey (10)], this estimation would yield ∼200 Purkinje cells per layer for the 100-μm fiber and ∼1,300 Purkinje cells per layer for the 600-μm fiber at 20 mW/mm$^2$. For irradiance of 60 mW/mm$^2$ (used to study CN responses), the volume receiving enough light to activate Purkinje cells had a radial extension of 1 mm and maximal depth of 1.5 mm (with thus ∼3,000 Purkinje cells per layer activated), whereas the volume exposed to intensities above 10 mW/mm$^2$ (which provides a conservative volume where depolarization block may occur) has a radial extension of 450 μm and maximal depth of 750 μm, and thus represents only ∼10% of the activated volume. The 60 mW/mm$^2$ condition will thus increase the volume stimulated by a factor of 5 compared to the 20 mW/mm$^2$ condition.

Because we computed the widest intersection of a planar Purkinje-cell layer, these numbers provide only order-of-magnitude estimates and not accurate numerical predictions; depending on the recording site, the topology of the lobule may bring one or two layers within the photostimulated volume. Therefore, we may consider that with a 100-μm fiber, we will activate 200–500 Purkinje cells whereas these numbers may be closer to 1,000–3,000 Purkinje cells with a 600-μm optic fiber at 20 mW/mm$^2$ and 5,000–10,000 Purkinje cells at 60 mW/mm$^2$.

**CN Data Analysis.** Single units were isolated as described previously (4, 11). Briefly, spikes were detected by thresholding of a high-pass filtered version (1 kHz) of the continuous recording, and the

main parameters of their waveforms were extracted. The data were then hand clustered by polygon-cutting in 2-dimensional projections of the parameter space using Xclust (Matt Wilson, Massachusetts Institute of Technology, Cambridge, MA). The quality of clustering was evaluated by inspecting the autocorrelograms of the units. To assess the presence of inhibition and to quantify its intensity, we applied more than 150 light pulses of various durations and intensities at 1 Hz or 0.3 Hz. Peri-stimulus-histograms (PSTHs) with bins of 2 ms were constructed. The latency to full inhibition corresponded to the time to the first empty bin after light onset, and the duration of full inhibition was obtained by counting the empty bins during or immediately after the light pulse. The instantaneous frequency was computed for each time bin (5 ms) by computing the geometric mean of the inverse of the interspikes interval that preceded all of the spikes occurring within this time bin. The ability of rhythmic trains of light pulses to constrain the firing of CN units is reflected by the presence of oscillations in the PSTHs during the stimulation. We therefore computed the power spectral density of PSTHs from experiments with 20 pulses of 12 ms and irradiance of 16.6 mW/mm$^2$ at 20 Hz/30 Hz; the peak value in the spectrum was normalized to the total power in the 0- to 100-Hz window.

**Statistical Analysis.** Means are given ± SD in the text unless otherwise stated. See figure legends for statistics in figures. Significance levels are indicated in figures as follows: (*) $P < 0.05$, (**) $P < 0.01$, (***) $P < 0.001$. The parameters (onset, offset, response rate) of the light-evoked CSs were obtained from the density of spikes convolved with a Gaussian kernel with a 20-ms variance; this convolution provides a curve similar to a peri-stimulus histogram with bin 20 ms; the baseline average (1 s before stimulation) was substracted from the spike density and the result was divided by the SD of the baseline. Significant departure from baseline over a search period T was detected when this studentized spike density departed by more than a z-score critical value corresponding to $P = 0.05/(T/bin)$. We used a search period starting at light onset and ending 250 ms after the light offset. The response rate is defined as the number of CS observed during the identified time interval of significant deviation from baseline, divided by the number of trial. For the study of the dependence of the timing of CSs to the recent history of CS firing (Fig. 4*D*), we constructed, for each cell in which CS frequency was above 0.1 Hz and for which at least 20 light-evoked CS were recorded, a PSTH aligned to the first CS response in each trial (with a response). Shuffled PSTHs were obtained by shifting each trial with a random number in the interval (−0.3; 0.3) ms. The average PSTHs were then compared with the average of 300 shuffled PSTHs.

**Immunochemistry.** Mice were perfused with 4% paraformaldehyde, and their brains were postfixed in 4% paraformaldehyde overnight. Sagittal Slices of 35 μm thickness were cut with a vibratome (Leica VT1000). Sections were washed three time with PBS and non-specific staining was blocked for 24 h using PBS contaning 1% BSA, 4% normal goat serum, and 0.5% triton. Slices were incubated for 48 h at 4 °C with the following antibodies: mouse anti-calbindin monoclonal antibody (1:1,000; Sigma Aldrich) and rabbit anti-GABA polyclonal antibody (1:1,000; Sigma Aldrich). Then sections were washed with PBS (5 × 10 min) and incubated for 2 h at room temperature with Alexa Fluor 633-conjugated goat anti-rabbit antibody (1:500; Invitrogen) and Alexa Fluor 555-conjugated goat anti-mice antibody (1:500; Invitrogen).


1. Gong S, et al. (2003) A gene expression atlas of the central nervous system based on bacterial artificial chromosomes. *Nature* 425(6961):917–925.
2. Valera AM, Doussau F, Poulain B, Barbour B, Isope P (2012) Adaptation of granule cell to Purkinje cell synapses to high-frequency transmission. *J Neurosci* 32(9):3267–3280.
3. Dugué GP, Dumoulin A, Triller A, Dieudonné S (2005) Target-dependent use of co-released inhibitory transmitters at central synapses. *J Neurosci* 25(28):6490–6498.
4. Pinault D (1996) A novel single-cell staining procedure performed in vivo under electrophysiological control: Morpho-functional features of juxtacellularly labeled thalamic cells and other central neurons with biocytin or Neurobiotin. *J Neurosci Methods* 65(2):113–136.
5. Garcia S, Fourcaud-Trocmé N (2009) OpenElectrophy: An electrophysiological data- and analysis-sharing framework. *Front Neuroinform* 3:14.
6. Gao H, Solages Cd, Lena C (2012) Tetrode recordings in the cerebellar cortex. *J Physiol Paris* 106(3-4):128–136.
7. Huber D, et al. (2008) Sparse optical microstimulation in barrel cortex drives learned behaviour in freely moving mice. *Nature* 451(7174):61–64.
8. Sultan F, Braitenberg V (1993) Shapes and sizes of different mammalian cerebella. A study in quantitative comparative neuroanatomy. *J Hirnforsch* 34(1):79–92.
9. Van Essen DC (2002) Surface-based atlases of cerebellar cortex in the human, macaque, and mouse. *Ann N Y Acad Sci* 978:468–479.
10. Napper RM, Harvey RJ (1988) Quantitative study of the Purkinje cell dendritic spines in the rat cerebellum. *J Comp Neurol* 274(2):158–167.
11. de Solages C, et al. (2008) High-frequency organization and synchrony of activity in the purkinje cell layer of the cerebellum. *Neuron* 58(5):775–788.

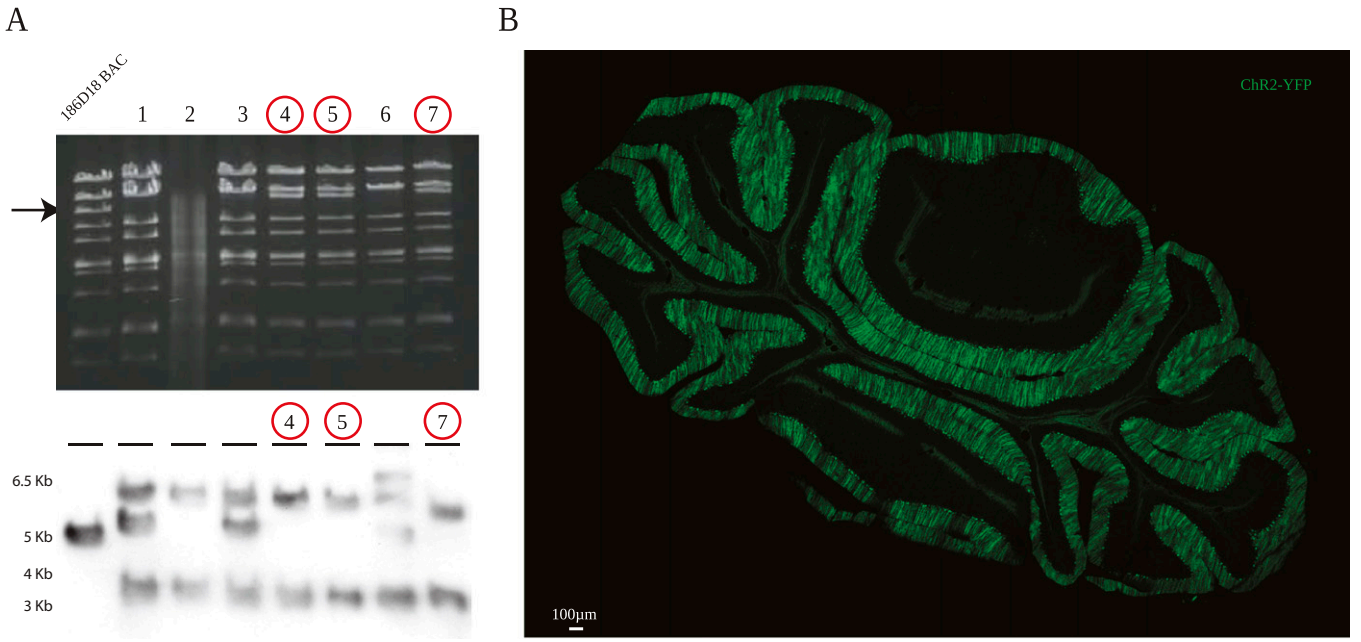


**Fig. S1.** Construction of L7-ChR2(H134R)-eYFP mice. (*A*) Pulsed-field gel analysis (*Upper*) of SpeI-digested BAC DNA confirmed correct insertion of the shuttle vector at the level of the *pcp2* ATG starting codon in exon 2 and ruled out major reorganization of the BAC (only one band shifted compared with the profile of the original BAC vector 186D18, arrow). Correct insertion of the shuttle vector was also checked by Southern blot analysis (*Lower*) using the homology box as a probe (SB probe, Fig. 1) and EcoRI-digested BAC DNA. The correctly recombined clones are circled in red. (*B*) L7-ChR2(H134R)-eYFP expression in cerebellar sections at P40 (50 µm).

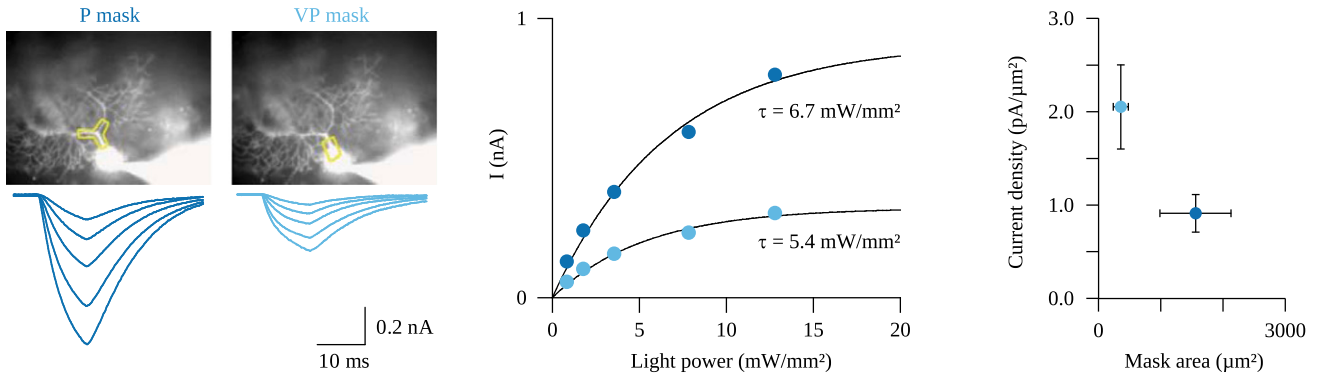


**Fig. S2.** Density of ChR2 currents in L7-ChR2(H134R)-eYFP Purkinje cells. (*Left*) Representative whole-cell recording from one PC. Currents evoked by 10 ms illumination (460 nm LED) at increasing irradiances (0.83, 1.79, 3.56, 7.84, and 12.80 mW/mm$^2$) over spatial patterns (masks) defined by a digital micromirror device (Mosaic; Andor Technology). The positions of proximal (P) and very proximal (VP) masks were verified by using a mirror slide, and their contours are shown over the recorded PC (loaded with Alexa 568). (*Center*) A 10-ms illumination peak current and their exponential fit plotted against irradiance for the two masks. (*Right*) Density current recorded using the two masks.

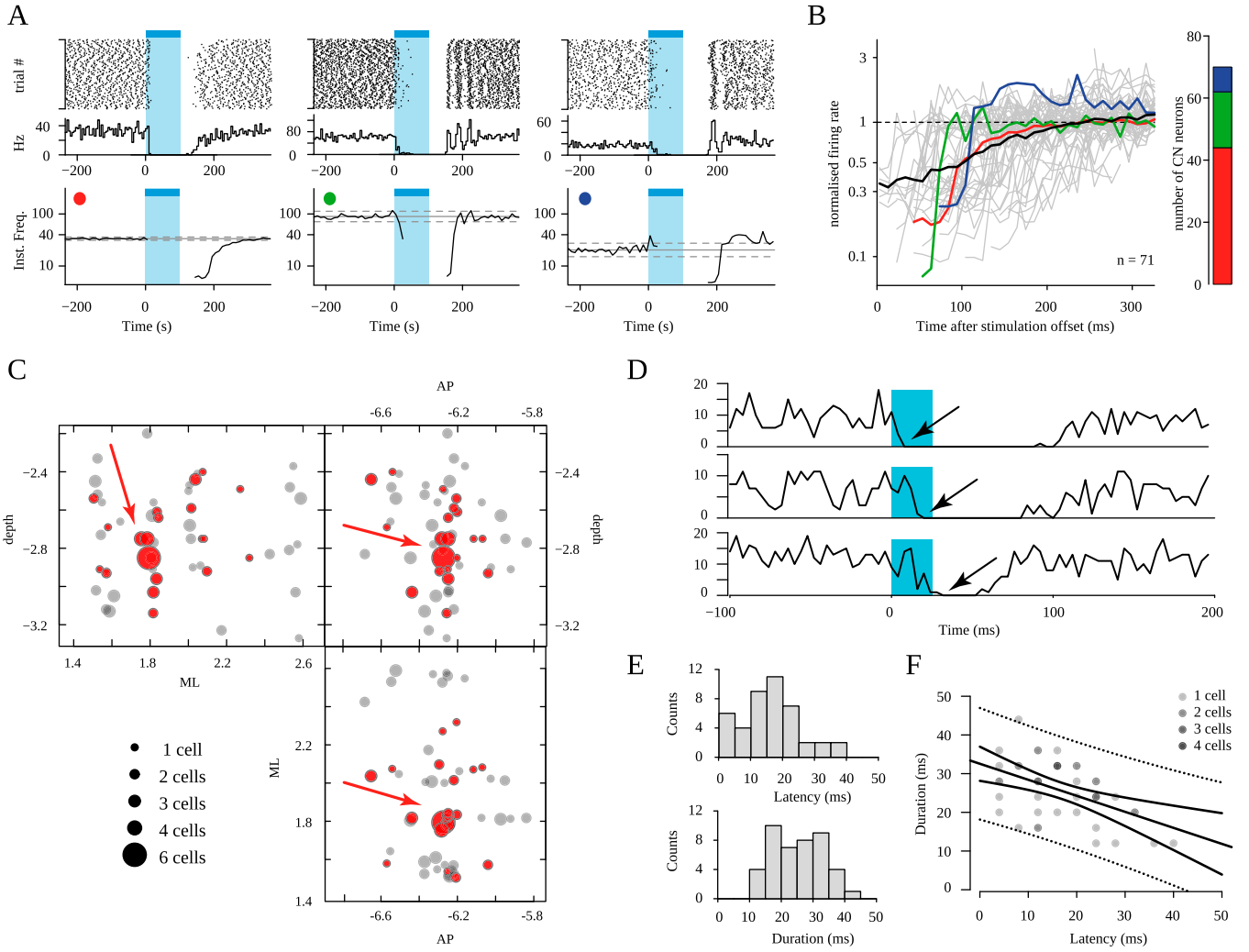


**Fig. S3.** Temporal and spatial properties of the light-triggered inhibition of cerebellar nuclear neurons. (*A* and *B*) Postsuppression firing behavior of cerebellar nuclear cells following photostimulation of Purkinje cells. (*A*) Three examples of cells displaying complete suppression of their firing in response to illumination of the ipsilateral Crus I region (100-ms light pulses, 60 mW/mm$^2$). For each cell, a raster plot (*Upper*) is represented on top of the corresponding PSTH (*Center*; bin, 5 ms) and average instantaneous frequency profile (*Lower*; bin, 10 ms; gray lines correspond to mean ± 2 SD of the baseline values). Unlike the first cell (red dot), the two other cells (green and blue dot) readily resumed their firing with a strong locking relative to the stimulation. However, only the third cell (blue dot) exhibited a modest but significant peak in the instantaneous frequency, suggestive of a postsuppression "rebound excitation." (*B*) Superimposed (gray) and average (black) instantaneous frequency traces of 70 cells during the postsuppression period (bin, 10 ms). Traces from example cells are plotted in red, green, and blue, respectively. The bar graph summarizes the distribution of the cells in the three categories depending on their postinhibitory behavior: no rebound and progressive return to baseline firing rate (red, $n = 44$); no rebound and time-locked return to baseline firing (green, $n = 18$); rebound (blue, $n = 8$). (*C*) Distribution of the coordinates of CN recording sites where inhibited cells were found (red) or not (black) during illumination of the ipsilateral cerebellar Crus I region [antero-posterior (AP), 6.1; medio-lateral (ML), 3.3; pulse = 100 ms, irradiance = 19 mW/mm$^2$]. The number of cell recorded at each site is represented as the diameter of the points. The red arrow identifies the region where most responsive sites are clustered. See Fig. 3G for a 3D view of the same data. (*D*) Examples of peri-stimulus histograms from three different CN neurons with latency to full inhibition (black arrow) smaller than 10 ms, between 10 and 20 ms, and longer than 20 ms, from top to bottom panels respectively (25 ms, 19 mW/mm$^2$, bin = 4 ms). (*E*) Histograms showing the distribution of latency and duration of full inhibition (for 43 cells, 25 ms, 19 mW/mm$^2$, bin = 4ms). (*F*) Plot showing the anti-correlation of these response parameters (linear fit: $r^2 = 0.24$, $P = 8.10^{-4}$).

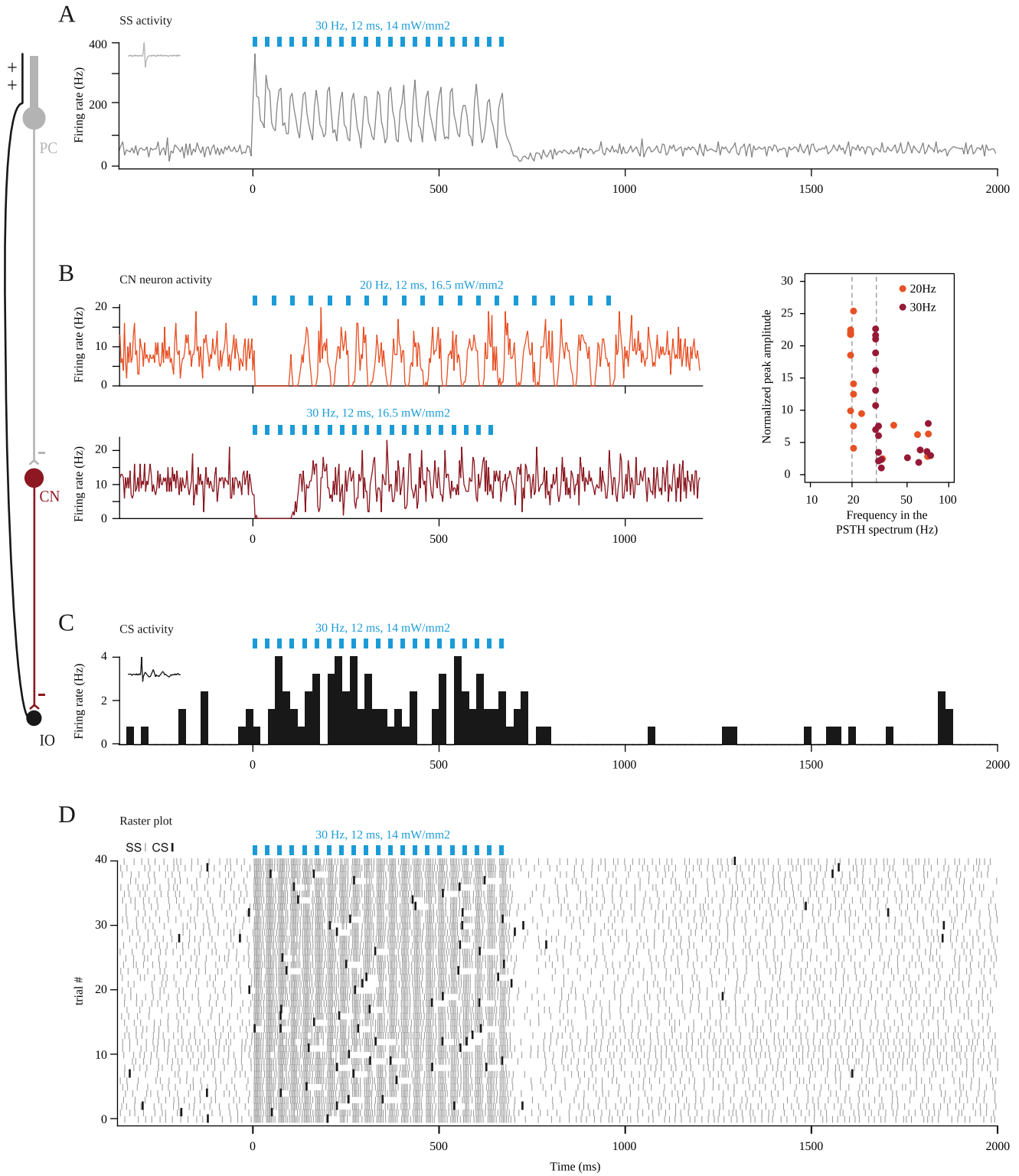


**Fig. S4.** Burst of light pulses elicits CSs in PCs in vivo. (*A*) Simple spike PSTH in one PC (bin: 5 ms) during 30 Hz illumination (12 ms light pulse, 14 mW/mm$^2$, blue bars). (*B*, *Left*) PSTH of one CN neuron (bin: 1 ms) in response to trains of illuminations (12-ms light pulses, 16.5 mW/mm$^2$, blue bars). After a short period of complete inhibition, the cell discharge was locked to the illumination pulses. (*Right*) For all 22 cells tested with stimulations pulses, the power spectral density of the PSTH (*SI Methods*) was calculated during the illumination; the presence of a peak at the same frequency as the stimulation evidences a time-locked inhibition of the cells. (*C*) PSTH of light-induced CSs in a PC (bin: 20 ms) during 30-Hz stimulation (same stimulation and same cell as in *A*). (*D*) Raster plot of simple spikes (gray ticks) and CS (black ticks) activity during 30-Hz stimulation of the cell in *A* and *C*. CN and PC are recordings from different set of experiments.

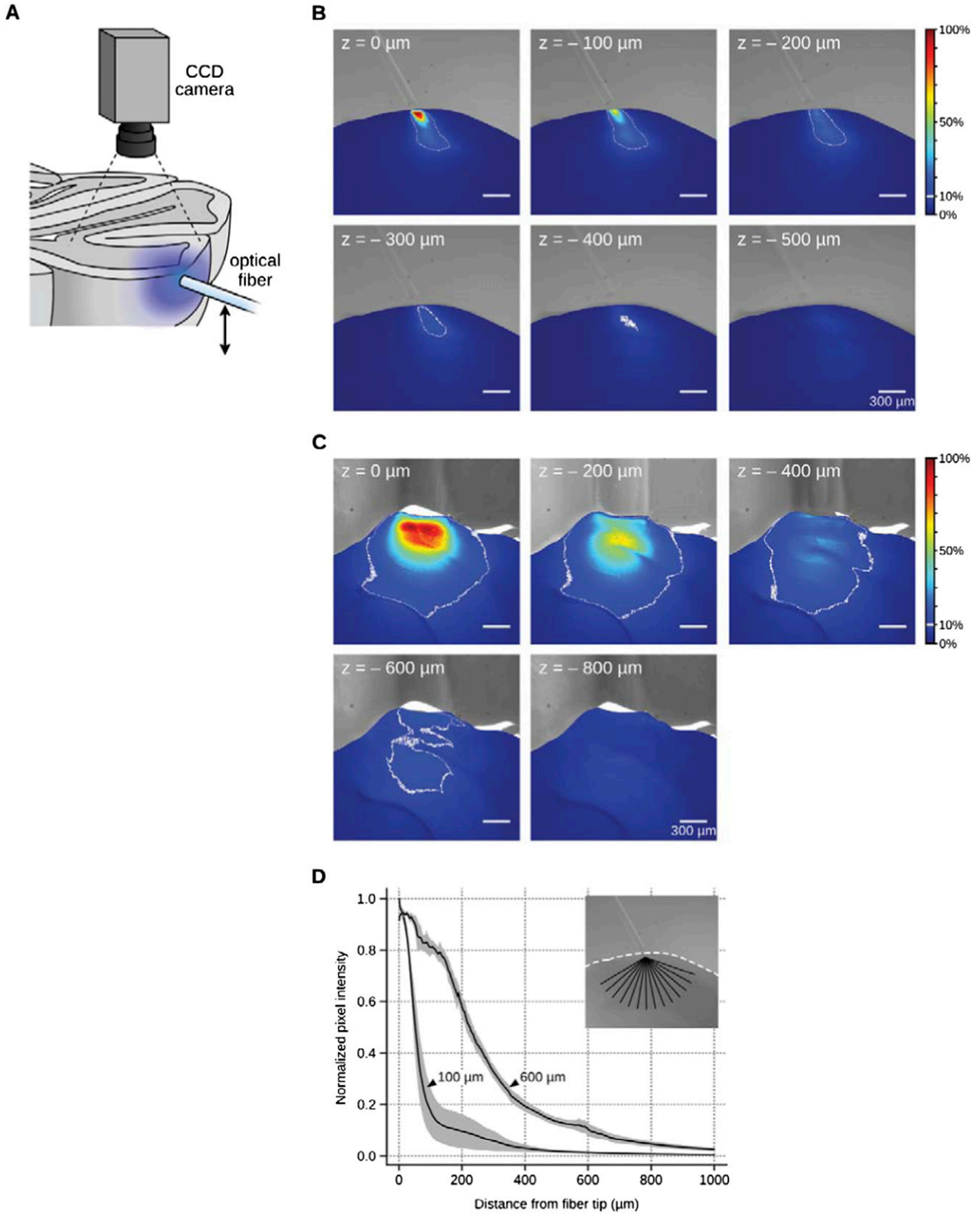


**Fig. S5.** Light power density mapping using cerebellar hemisections. (*A*) Schematic of the experimental setup. The cut surface was imaged from the top using a CCD camera whereas the tissue was illuminated from the side through an optical fiber coupled to blue (470 nm) LED. The fiber was translated vertically (two headed arrow) to assess the lateral propagation of light. (*B*) Series of images taken for different vertical fiber positions using a 100-µm optical fiber with an angle of incidence of ~30° and a distance to the *pia* of around 100 µm. The position of the fiber relative to the cut surface is indicated in white. Pictures were taken in the dark with a power at the fiber tip of 125 µW. The intensity of each pixel is expressed as a percentage of the intensity of the brightest pixel of the image series and color coded. The 10% isoline is delineated in white on each image. The color-coded image of the tissue is superimposed on a grayscale picture

Legend continued on following page

of the fiber obtained with a brightfield side illumination. Here, the hemisection was done coronally. (*C*) A similar series of images taken for different vertical fiber positions, using a 600-μm optical fiber. Here, the fiber was affixed perpendicularly to the *pia*, and the hemisection was performed parasagitally. The power at the fiber tip was 200 μW. The white patches in the grayscale picture are due to reflections of the brightfield side illumination on the surface of the liquid. (*D*) Decay of the pixel intensity as a function of distance from the brightest pixel. Pixel intensity profiles were measured for the upper fiber position (z = 0 μm) along 70 evenly distributed lines drawn through the tissue. All lines originated from the brightest pixel underneath the fiber tip (as indicated in the top right *Inset*). The average curves calculated from these profiles are plotted for the experiments shown in *B* and *C*. Note the much steeper decay of pixel intensity for the 100-μm fiber. The shaded area represents the SD for the 70 profiles along the lines radiating from the most intense pixel.

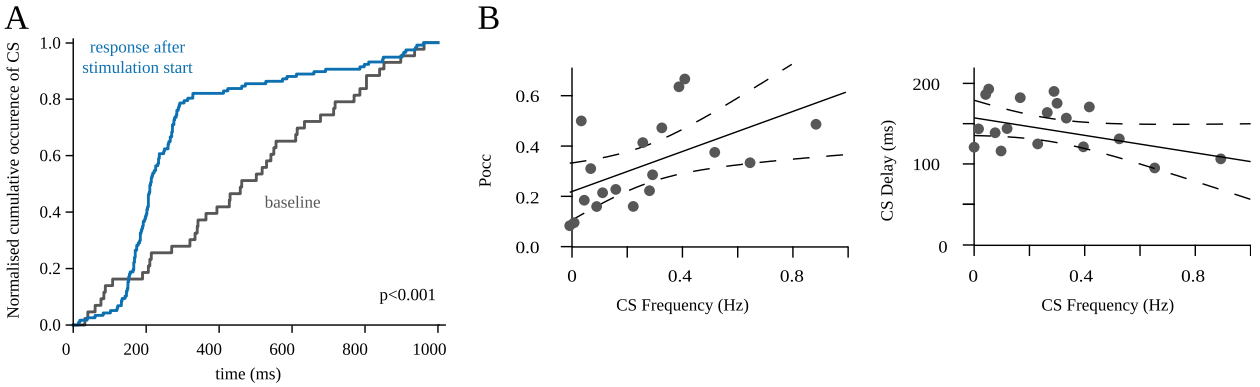


**Fig. S6.** Purkinje-cell synchronization triggers complex spike responses. (*A*) Normalized cumulative PSTH of light-induced CS for one cell (bin: 2ms) during 1 s before (gray) and after stimulation start (blue). Cumulative PSTHs were significantly different for 25/42 PCs (Kolmogorov–Smirnov; $P < 0.001$). (*B*) Scatter plot of the probability of occurrence (Pocc, *Left*) or the delay (*Right*) of the light-induced CSs as a function of the baseline CS firing rate.